Magneto-straintronics on a Co-coordinating metalloboronfullerene

Jing Liu,[1] Yiming Zhang,[2] Chun Li,[2,3,*] Wei Jin,[4] Georgios Lefkidis,[1,2] and Wolfgang Hübner[1]

[1]*Department of Physics and Research Center OPTIMAS, University of Kaiserslautern, PO Box 3049, 67653 Kaiserslautern, Germany*

[2]*School of Mechanics, Civil Engineering and Architecture, Northwestern Polytechnical University, Xi'an 710072, China*

[3]*Department of Mechanical Engineering, University of Manitoba, Winnipeg, Manitoba R3T 5V6, Canada*

[4]*School of Physics and Information Technology, Shaanxi Normal University, Xi'an 710119, China*

(Received 7 October 2019; revised 18 June 2020; accepted 22 June 2020; published 13 July 2020)

The strain-modulated ultrafast spin dynamics of Co embedded exohedral boron fullerene $[Co\&B_{40}]^-$ is investigated with high-level *ab initio* calculations. We find that due to its high ductility and malleability, B_{40} can retain its structure upon both the addition of a magnetic atom and the exertion of mechanical tensile or compressive strain, and that its elasticity modulus is highly anisotropic. The geometric optimization reveals that $[Co\&B_{40}]^-$ prefers three different configurations. For the spin-dynamics investigation we focus on one of them, namely the configuration with the Co located near the center of a heptagon (the only geometry in which the boron cage remains intact) as an example to investigate the spin-dynamics features. Several laser-induced spin-flip scenarios are suggested, the details of which strongly depend on the magnitude and the direction of any deformations. Thus, utilizing the coupling between the external mechanical strain and the spin degree of freedom in magnetic exohedral all-boron fullerenes, we demonstrate the realizability of magnetostraintronic devices on molecular systems. The asymmetric modulation of the spin-flip process with respect to the tensile and compressive strain (tension-compression-asymmetric ultrafast spin dynamics) can provide further control of such integrated spin-logic devices.

DOI: 10.1103/PhysRevB.102.024416

I. INTRODUCTION

Since the demonstration that structural distortion can significantly modify the electric or magnetic properties of bulk crystals [1–4], thin films [5–8], or even single molecules [9–13], strain engineering and straintronic mechanism has grown into an intriguing area of research that can be used to improve the performance of electronic devices [14–19]. Specifically, the possibility to manipulate the electronic spin state and spin dynamic features through the external strain or the change of the geometric configuration has been confirmed in different materials [3,4,20,21]. One can see that the coupling between electronic spin and structural deformation is of strong promise for realizing unprecedented quantum information processing schemes. At the same time, with the increasing demand for the miniaturization of computer processors, magnetic molecules and nanoscale clusters hold great potential as candidates for the future spintronic devices due to their small size. The discrete levels and the highly localized spin density of molecular systems are instrumental in achieving controllable spin dynamics. In addition, several experiments already address the technical difficulty of inducing and detecting structural deformation on molecular systems by using atomic force microscopy (AFM). For example, Xu *et al.* demonstrated that the deformation of molecule electrode junctions can be performed by moving an Au-coated Si tip mounted on an atomic force microscope [22]; Frei *et al.* provided an experimental method to induce and detect the relative length modification of molecular junctions [23]; Habid *et al.* systematically investigated the intramolecular strain in the alkanedithiol and alkanediamine molecular families and explored how a strain applied to the junction is dispersed among the molecular bonds [24]. These studies clearly indicate the possibility of controlling the spin degree of freedom with external strain in microscopic systems such as molecules.

Nowadays, single molecules and nanoparticles have taken over an important role in the design of novel nanoscale devices and applications [25,26]. Among the multiple materials with possibly intriguing spin features, endohedral, and exohedral fullerenes have their own merits [27]. Their structural robustness and the long coherence time of their electronic states enables them to serve as functional information carriers, while their high ductility provides a wide nondestructive deformation window [28]. In 2010, Popov and his colleagues have revealed the coupling effect between the spin flow and the cluster vibration in $TiSc_2@C_{80}$ [12]. Following this, other studies on the interaction between structural deformation and spin properties of different fullerene systems were also performed [29,30].

Initially the investigations of strain engineering and electronic spin properties focused mainly on carbon fullerenes. However, the noncarbon fullerenes also start to attract more and more interest [31–33]. As one of the closest elements to carbon in the periodic table of elements, boron seems to be the best candidate. Experimental detection of the rather small fullerene-like cage cluster B_{40} was reported by Zhai *et al.* in 2014 [34]. Particularly, there was a significant distinction between the geometric configurations of B_{40} and typical fullerene structures. Carbon fullerenes are usually composed

*lichun@nwpu.edu.cn

of hexagons and pentagons, while B_{40} consists of four heptagons on its waist and two hexagons at the top and the bottom (following Zhai, we refer to this fullerene-like cage also as fullerene). The diameter of the hollow sphere inside B_{40} is about 6.2 Å, which is large enough to hold a metal atom or a small cluster to produce various endohedral and exohedral fullerenes [35–38]. Several intriguing features of B_{40} and its metalized derivatives, such as high hydrogen storage capacity [39,40], high sensitivity for NH_3 detection [41,42], and high CO_2 adsorbivity [43,44], have also been predicted. However, to the best of our knowledge, there is still no investigation on the spin dynamic properties and the coupling effect between spin and external stimuli, such as magnetic fields, laser pulses, and strain, in boron fullerenes.

To investigate the strain effect on the spin-dynamics behavior of such boron fullerene systems, the pristine B_{40} subjected to uniaxial stretching and compression are investigated first to explore the feasibility and the deformation characteristics of the molecule. Then the laser-induced ultrafast spin-switching mechanism of $[Co\&B_{40}]^-$ and the strain effect on the spin-switching process in different configurations are investigated in detail. It is found that $[Co\&B_{40}]^-$ prefers the configuration with the Co located near the center of heptagon, slightly outside the boron cage. The spin switching on $[Co\&B_{40}]^-$ can be accomplished on the subpicosecond timescale. In particular, the dynamic features of the spin-switching process on the structures can be manipulated by applying uniaxial strain. Utilizing the coupling of the mechanical deformation and the spin degree of freedom, such tension-compression-asymmetric ultrafast spin dynamics provides new possibilities for the design of a spin device based on the metalloboron-fullerenes.

II. THEORY AND METHODS

The stability and ductility of the pure B_{40} molecule is investigated first by using both density functional theory (DFT) and Hartree-Fock (HF) methods. The HF calculations are necessary since our spin-dynamics calculations are based on correlated post-HF methods, while the DFT calculations are used to compare and validate the HF geometries. The stability of the structures is verified by the absence of vibrational modes with imaginary frequencies. The convergence criteria for the geometry optimization are set as follows: (i) the maximum component of the force must be below the cutoff value of 4.5×10^{-4} Ha/a_0 (a_0 is the Bohr radius), (ii) the root-mean-square of the forces must be lower than 3.0×10^{-4} Ha/a_0. Based on the optimized structure, the elastic properties of B_{40} are examined and the values of the elastic constants are obtained by analyzing the potential energy curve (PEC). The geometry optimization of both the equilibrium and distorted $[Co\&B_{40}]^-$ is performed with the restricted open-shell Hartree-Fock (ROHF) method (to allow for the subsequently employed post-HF methods, which necessitate restricted molecular orbitals), and the electronic many-body states are obtained with the high-level symmetry-adapted cluster configuration interaction (SAC-CI) method as implemented in the GAUSSIAN quantum-chemistry package [45,46]. In the SAC-CI method, the many-body wave functions are represented by a cumulative expansion of the virtual excitations. The correlated wave function of the ground state is given by

$$|\Phi_g\rangle = e^{c_I\hat{S}_I + c_J\hat{S}_J + \cdots}|\Phi_{\mathrm{HF}}\rangle = \left(1 + \sum_I c_I\hat{S}_I + \frac{1}{2}\sum_{IJ} c_I c_J \hat{S}_I\hat{S}_J + \cdots\right)|\Phi_{\mathrm{HF}}\rangle, \quad (1)$$

where $\hat{S}_I$ and $\hat{S}_J$ symbolically denote symmetry-adapted excitation operators (e.g., single or double excitation operators), and c_I and c_J are their respective amplitudes. $|\Phi_{\mathrm{HF}}\rangle$ is the Hartree-Fock configuration. For the excited states, the wave functions are represented by

$$|\Phi_e\rangle = \sum_K d_K\hat{R}_K|\Phi_g\rangle - \sum_K \langle\Phi_g|d_K\hat{R}_K|\Phi_g\rangle\,|\Phi_g\rangle, \quad (2)$$

where the $\hat{R}_K$ denote the excitation operators acting on the ground state $|\Phi_g\rangle$, and d_K are their respective coefficients. It should be noted that all single excitation operators are included, while only double virtual excitations with second-order energy contributions larger than 10^{-6} Ha are considered. Notably, SAC-CI is a size consistent method suitable for problems involving geometry alterations, such as strain and deformation [47]. For the Co atom the Los Alamos National Laboratory with double zeta basis set (LANL2dz) with effective core potentials (ECP) is used [48]. For the B atoms we use three different basis sets, namely STO-3G, 6-311G, and 6-311+G*. Due to the multitude of structures and geometries needed for our study (and the high computational costs for each structure as well), we restrict ourselves to the lower-quality basis set for the majority of our spin-dynamics scenarios. However, the validity of those results is verified by comparing for a number of representative cases with the results obtained from the higher-quality basis sets (6-311G and 6-311+G*). The comparison comprises the optimized geometry and the spin-density localization of the molecules.

The spin dynamics of our Co-doped B_{40} system is based on optical Λ processes [49–51]. A Λ process is a laser-induced transition of a system from an initial electronic state to a final electronic state with opposite spin direction (as shown in Fig. 1). The transition happens in two steps: an excitation from the initial state to an electronically higher-lying spin-mixed intermediate state, followed by a deexcitation from the intermediate state to the final state. Although this is a two-photon process, it often proves to be considerably faster than a direct process (if the latter one is forbidden, as is the case with the spin-flip processes, since it would necessitate the much slower magnetic-dipole transitions). The initial and the final states are usually (quasi)degenerate and therefore an external magnetic field is necessary both to differentiate them and to set the magnetization axis. The spin-mixing of the intermediate state is, in our case, due to spin-orbit coupling (SOC).

Generally, the intermediate C states are quantum superpositions of the $S_z = 1$ and $S_z = -1$ substates of triplet states with $\langle C|\hat{S}_z|C\rangle \approx 0$ (a condition required by the optical selection rules for the case of the electric-dipole approximation [49,52,53]), often also combined with singlet states (note that in the case of electrons, SOC can mix singlets with triplet states through the $\hat{S}_z$ operator). Pure-spin states can also function as intermediate states in the case of spin-transfer

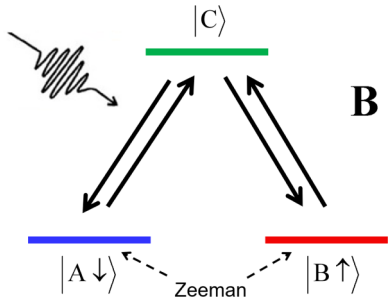

FIG. 1. The Λ process. The electronic states $|A\downarrow\rangle$ and $|B\uparrow\rangle$ are the two (quasi)degenerate states with opposite spin directions. ↓ and ↑ denote spin-down and spin-up states, respectively. State $|C\rangle$ is energetically far away from $|A\downarrow\rangle$ and $|B\uparrow\rangle$, and optically addressable from both of them. An external static magnetic field **B** induces a Zeeman splitting between $|A\downarrow\rangle$ and $|B\uparrow\rangle$. A suitably tailored laser pulse excites the system from state $|A\downarrow\rangle$ to an intermediate spin-mixed state $|C\rangle$ and then deexcites it to state $|B\uparrow\rangle$.

processes. Numerous such Λ processes have already been studied on surfaces [50], clusters [54], and endohedral carbon fullerenes [30].

On top of the many-body states obtained by SAC-CI calculations, the SOC and a static magnetic field (Zeeman splitting) are perturbatively added. The corresponding Hamiltonian is

$$\hat{H}_{\mathrm{SOC}} = \sum_{i=1}^{n} \frac{Z_a^{\mathrm{eff}}}{2c^2 R_i^3} \hat{\mathbf{L}} \cdot \hat{\mathbf{S}} + \sum_{i=1}^{n} \mu_{\mathrm{L}} \hat{\mathbf{L}} \cdot \mathbf{B}_{\mathrm{stat}} + \sum_{i=1}^{n} \mu_{\mathrm{S}} \hat{\mathbf{S}} \cdot \mathbf{B}_{\mathrm{stat}}, \tag{3}$$

where $\hat{\mathbf{S}}$ and $\hat{\mathbf{L}}$ are the spin and the orbital angular momentum operators, respectively. μ_{L} and μ_{S} are their respective gyromagnetic ratios. Z_a^{eff} denotes the relativistic effective nuclear charges which account for the two-electron contributions to the SOC. $\mathbf{B}_{\mathrm{stat}}$ is the static external magnetic field, and c denotes the speed of light.

To describe the spin-dynamics process on $[\mathrm{Co\&B_{40}}]^-$, the well-selected many-body states are propagated in time under the influence of a sech^2-shaped laser pulse. The time-dependent Hamiltonian reads

$$\hat{H}'(t) = \hat{\mathbf{D}} \cdot \mathbf{E}_{\mathrm{laser}}(t) + \mu_{\mathrm{S}} \hat{\mathbf{S}} \cdot \mathbf{B}_{\mathrm{laser}}(t) + \mu_{\mathrm{L}} \hat{\mathbf{L}} \cdot \mathbf{B}_{\mathrm{laser}}(t), \tag{4}$$

where $\mathbf{E}_{\mathrm{laser}}(t)$ and $\mathbf{B}_{\mathrm{laser}}(t)$ are the electric and magnetic fields of the laser pulse, respectively, and $\hat{\mathbf{D}}$ is the electric-dipole-transition operator. The propagation of the of many-body wave functions is described by the coupled differential equations

$$\frac{\partial c_n(t)}{\partial t} = -\frac{i}{\hbar} \sum_k \langle \Phi_n | \hat{H}'(t) | \Phi_k \rangle c_k(t) e^{-\frac{i(E_k - E_n)t}{\hbar}}, \tag{5}$$

where $|\Phi_n\rangle$ and $|\Phi_k\rangle$ are the unperturbed eigenstates of $\hat{H}_{\mathrm{SOC}}$, c_n is the complex scalar coefficient of the nth in the wave function $\Psi(t) = \sum_n c_n(t) e^{-iE_n t/\hbar} |\Phi_n\rangle$. E_n and E_k are the energies of the nth and kth states, respectively. $\hbar$ is the reduced Planck's constant.

The parameters of the laser pulses are optimized with a specially developed, largely flexible genetic algorithm [55]. The quality of each spin manipulation process is given by its fidelity, defined as the projection of the actual final state after the pulse on the desired state. In our case, since our desired states are always pure states, the fidelity is simply given by the final population of the desired state.

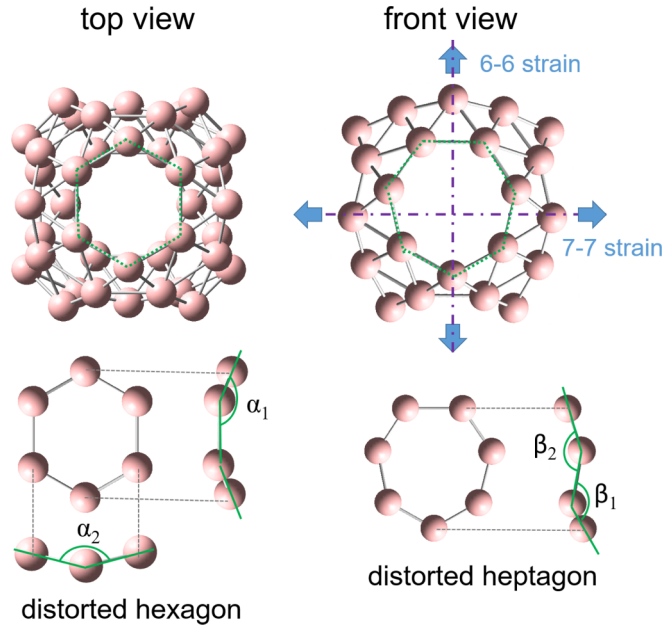

FIG. 2. Optimized B_{40} structure. The top panels show the top and front view of B_{40}. The blue arrows show the direction of the applied strain. The hexagon and heptagon on the surface of B_{40} are shown by green dotted lines. The bottom panels show the bent hexagon and heptagon structure. The dihedral angles α_1, α_2, β_1, and β_2 are shown as well.

III. RESULTS AND DISCUSSION

A. Structural optimization and mechanical properties of B_{40}

The optimization of the pure B_{40} is performed first. The DFT calculations, which can converge more easily than the HF ones, are done with the 6-311+G* basis set at the PBE0 level (the same as what Zhai *et al.* used [34]). Since our subsequent investigations on the spin-dynamics on the Co-doped B_{40} are based on post-HF methods, the HF calculations are also performed for comparison with two basis sets: STO-3G and 6-311G. All optimization calculations of the pure B_{40} cage converge to a similar geometry, which belongs to the D_{2d} point group (Fig. 2, top panel). The average B-B bond lengths calculated with the HF method and the 6-311G and STO-3G basis sets are 1.702 Å and 1.669 Å, respectively, while the DFT calculation delivers a value of 1.684 Å. In all calculations the heptagons and hexagons on the surface of B_{40} are slightly distorted, which is consistent with Zhai's results. The dihedral angles on the distorted hexagons and heptagons are shown in Table I and Fig. 2. The differences resulting from the two methods and the three basis sets range between 0.036° and 2.253°, and can be thus considered negligible. All detailed geometries are given in the Supplemental Material [56].

To investigate the elastic properties of B_{40}, external strain is applied statically along two typical directions: through the centers of two antipodal hexagons (6-6 direction) and through the centers of two antipodal heptagons (7-7 direction), which

TABLE I. Geometric parameters of optimized B_{40} structure. Bond length denotes the average value of B-B bond length. α_1, α_2, β_1, and β_2 denote the dihedral angles on the distorted hexagons and heptagons on the surface of B_{40}, which is shown in the bottom panel of Fig. 2.

		Bond	Dihedral angle			
Method	Basis set	length (Å)	α_1 (°)	α_2 (°)	β_1 (°)	β_2 (°)
PBE0	6-311+G*	1.684	157.751	153.502	151.467	147.746
HF	6-311G	1.702	159.955	155.755	150.797	148.351
	STO-3G	1.669	159.339	153.466	149.895	147.654

are shown by the blue arrows in the top panel of Fig. 2. The strain is increased in steps of 0.5% until the geometry of B_{40} collapses (the strain percentage refers to the change of the cage diameter along the strain axis, with respect to the undeformed system which is 5.575 Å). To compare to Zhai's work, here we show our results calculated with PBE0 and 6-311+G*. According to our calculations, the external strain along the 7-7 direction lowers the symmetry of the system to C_{2v}, while the strain applied along the 6-6 direction preserves the original D_{2d} symmetry. In addition, our results show that the maximal tensile and compressive strain along the 6-6 direction before material failure is 26.0% and −18.5%, respectively. As material failure we define the point at which the geometry of the system collapses to a visibly non-fullerene-like nanocluster. While for the deformation along the 7-7 direction, the maximal tensile and compressive strain is 17.0% and −15.0%, respectively. Note that the maximal strain calculated with the HF method (≈10.25%) is less than the DFT counterpart. The large ultimate strain of the pristine B_{40}, which corresponds to a maximum displacement of almost 1.45 Å, indicates its capacity to encapsulate or attach a large metal atom.

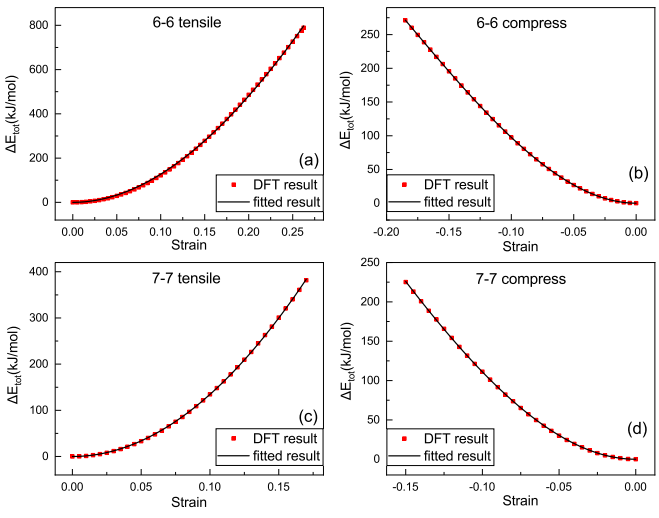

FIG. 3. The potential energy curve of B_{40} during (a), (c) uniaxial tensile and (b), (d) uniaxial compression processes. 6-6 and 7-7 denote the strain direction (along the centers of two hexagons and the centers of two heptagons, respectively). The red dots denote the DFT result. The black curve is the fitted result of Eq. (6)

TABLE II. Fitting result of Young's modulus E and nonlinear elastic constant D for both stretching and compression process.

Distortion	E (Nm^{-2})	D (Nm^{-3})	R^2
6-6 tensile	26942.017	−21717.274	0.99976
6-6 compressive	23777.764	64152.702	1.00000
7-7 tensile	27387.585	−16449.250	0.99996
7-7 compressive	26418.902	63362.663	0.99998

The relation between strain and total energy of the system is found by the near-equilibrium PECs, as shown in Fig. 3. The parameter ΔE_{tot} denotes the energy difference between the distorted and the equilibrium configurations (here we take the total energy of the equilibrium configuration as a reference). The overall elastic constants of the system are derived by fitting the PECs of Fig. 3 with the equation

$$\Delta E_{tot} = \frac{1}{2}E\varepsilon^2 + \frac{1}{3}D\varepsilon^3, \quad (6)$$

where ε denotes the strain magnitude. E and D are the linear Young's and the nonlinear elastic moduli, respectively. The fitting results are shown in Table II. All correlation coefficients R^2 surpass the value of 0.999. Specifically, the correlation coefficient for compression along the 6-6 direction even equals to 1 up to the fifth decimal digit, which strongly verifies the extremely high accuracy of the fitting. It also demonstrates that the uniaxial tension and compression on B_{40} are both nonlinear mechanical processes. Furthermore, a glance at the different values of E and D along the two directions reveals that the pristine B_{40} exhibits high elastic anisotropy, which mainly results from the specific D_{2h} symmetry of B_{40}.

B. Structural optimization and spin dynamics of $[Co\&B_{40}]^-$

We start from the stable structure of B_{40} and we embed a magnetic atom Co into the boron cage and then investigate the spin-dynamics properties of the whole magnetic metallofullerene system. We altogether construct 12 different initial configurations. Each configuration is geometrically fully relaxed at the ROHF level to obtain the equilibrium structure. In addition, three different ionization states (−1, 0, and +1) are also considered. Two distinct basis sets are chosen for the Co and B atoms: the Los Alamos basis set with relativistic effective core potentials (LANL2dz with ECP) is used for cobalt and STO-3G is used for boron, respectively. The combination of the SAC-CI method and the specific basis sets (LANL2dz ECP and STO-3G) has already been successfully used in our previous investigations on endohedral metallofullerene systems [30,57–59]. Finally, the optimization converges to the anionic molecule and yields three stable structures with Co sitting in three different positions (Fig. 4): (i) near the center of a heptagon (Hep-type), (ii) near the center of a hexagon (Hex-type), and (iii) near the center of the boron cage (C-type). Remarkably, The total energies of the three structures from the most to the least stable are: Hex-type (−30418.127 eV), C-type (−30416.522 eV), and Hep-type (−30414.937 eV). However, the boron cages of the Hex-type and C-type structures are so strongly deformed (shown in Fig. 4), that they cannot be regarded as a boron fullerenes any more. Therefore, we do not consider these two structures in

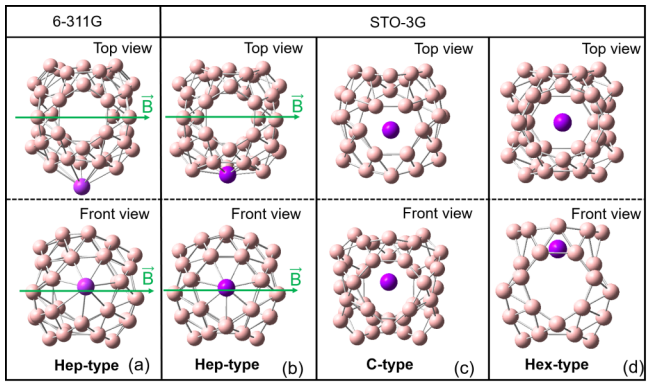

FIG. 4. Optimized $[Co\&B_{40}]^-$ structures. (a) Hep-type structure optimized with LANL2dz ECP for Co and 6-311G for B. (b) Hep-type, (c) C-type, and (d) Hex-type structures optimized with LANL2dz ECP for Co and STO-3G for B. Both front view and top view are shown. Pink balls are used to represent the boron atoms and a purple ball represents the cobalt atom. The green arrow shown in (a) indicates the direction of the external static magnetic field.

our subsequent investigations. As for the Hep-type structure, the Co atom is relaxed to a position near the center of a heptagon on the surface of B_{40} and slightly outside the boron cage, thus forming a exohedral metallofullerene $[Co\&B_{40}]^-$. This geometry is quite similar to the reported optimized Mg-doped B_{40} molecule [42]. The distance between the Co atom and the center of the heptagon is about 0.499 Å. The boron cage undergoes a modest distortion and its symmetry is reduced from D_{2d} for the pristine B_{40} to C_s for the endofullerene.

To investigate the spin dynamics, first the spin density distribution of $[Co\&B_{40}]^-$ is examined. To render the SAC-CI calculation manageable, a typical active window consisting of 161 molecular orbitals (MOs) is chosen (out of a total of 224 MOs), which is large enough to account for the $d \leftrightarrow d$ transitions of the Co atom. We find that the greatest part of the spin density of the energetically lowest triplet state (i.e., the first excited state) is localized on the Co atom with the value of 0.854 (the magnitude of the total spin density is 2.000), while the rest of spin density is almost equidistributed among all boron atoms, each one carrying only a very small portion of the spin density. In this respect, a global spin-flip is practically equivalent to a localized spin-switching process. When including SOC and an external static magnetic field [the magnitude is set to 2.35 T and the direction is denoted by the green arrow in Fig. 4(a)], the spin-up and spin-down substates of the first excited state, which is the lowest triplet state, are split with an energy difference of 1.032 meV. This satisfies the energy requirements for achieving a Λ process since it is large enough to make the two states distinguishable and in the meantime prolongs the lifetime of the energetically higher state by suppressing the direct relaxation processes between them [60]. Therefore, these two states are chosen as the initial and final states for a spin-switching process. It is noteworthy that the spin density of Co of the Hex-type and the C-type structures is 0.310 and 0.355, respectively (detailed information is shown in Table S8 of Supplemental Material [56]). The low spin density on the Co atom does not fulfill our demand for achieving a local spin-switching process (by "local" we mean on the metal atom). This is one more reason why we only consider the Hep-type structure for the subsequent investigations.

TABLE III. Optimized parameters of the laser pulse for each spin-switching process. θ and φ denote the angles of incidence in spherical coordinates and γ is the angle between the polarization of the light and the optical. The last column refers to the basis set used for B. For Co the LAND2dz basis set is used throughout this work.

strain	fidelity	θ (°)	φ (°)	γ (°)	Energy (eV)	basis set
0.0	0.965	187	135	177	0.712	6-311G
−1.0%	0.977	27	116	346	2.481	STO-3G
−0.5%	0.992	54	130	142	2.513	STO-3G
0.0	0.977	5	273	168	2.541	STO-3G
0.5%	0.998	61	89	159	2.433	STO-3G
1.0%	0.996	162	21	126	2.386	STO-3G

Before studying the spin-dynamics, we also perform the same calculations with a larger basis set (6-311G for B atoms and LANL2dz ECP for Co atom) to ensure the validity of the results based on the smaller basis set. After the full geometrical relaxation at the ROHF level, only one stable cage-like structure remains, again with the Co atom sitting outside the boron cage, near the center of the heptagon (Hep-type), shown in Fig. 4(a). This structure is geometrically similar to the aforementioned Hep-type structure optimized with the smaller basis set (STO-3G). However, the distance between the Co atom and the center of the heptagon (1.364 Å) is larger than the previous value (0.499 Å). The symmetry of the cage is reduced from the D_{2d} point group for the pristine B_{40} to the C_1 group for the Co-embedded cluster. The SAC-CI active window comprises 312 MOs out of a total of 544 MOs. The spin density of the triplet ground state is highly localized on the Co atom with an absolute value of 0.842 (the total spin density is 2.000), which once more is almost identical with the STO-3G results.

After the optimization of the laser pulse parameters (used for the spin-dynamics scenarios) with our genetic algorithm, we find successful laser-induced spin-switching processes on the aforementioned two Hep-type structures. The parameters of the laser pulses are given in Table III. The fidelity of each spin-switching process is larger than 95.00%. Figure 5 shows the time evolution of the population of each electronic state involved in the spin-switching process, as well as the spin components along the x, y, and z directions. Notably, in the illustrations of time evolution of population, only the initial and final states have consistent color (black and red), while the intermediate states are simply colored differently to make them more distinguishable from the initial and final states (the reason is that the number of the intermediate states differs from case to case). The beginning of the spin-switching process is identified by the breakdown of the initial steady state, while the switching process is considered completed when the population of the electronic states becomes steady again (no relaxation is taken into account since we are working within the coherent regime).

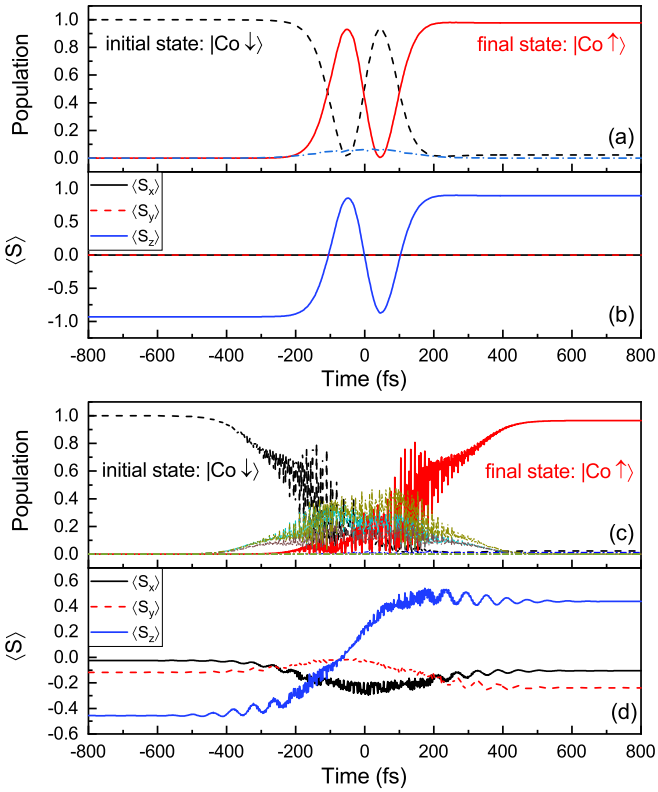

FIG. 5. Local spin-switching process achieved on Hep-type $[Co\&B_{40}]^-$. (a) and (b) denote the spin switching scenario on the structure optimized with LANL2dz for Co and STO-3G for B, (c) and (d) denote the spin switching scenario on the structure optimized with LANL2dz for Co and 6-311G for B. (a) and (c) are time evolution of electronic population of the initial (dashed black line), final (solid red line), and intermediate states [dash-dotted line in other colors, for example, the green and blue lines shown in (c) denote two highly populated intermediate states]. $|Co\downarrow\rangle$ and $|Co\uparrow\rangle$ denotes the spin-down (initial) and spin-up (final) states with the spin density highly localized on the Co atom. (b) and (d) are the time-resolved expectation values of the spin components.

As shown in Figs. 5(a) and 5(b), the spin-switching process completes within about 500 fs on the Hep-type $[Co\&B_{40}]^-$ optimized with LANL2dz and STO-3G basis sets. Note that there is only one intermediate state involved in the process with energy 2.422 eV higher than the initial state. Considering that the initial and final states are quasidegenerate, this spin-switching process can be regarded as a perfect Λ process. The intermediate state temporarily attains a maximum population of mere 0.066, although its presence is indispensable. This blocking effect has already been reported in other molecular magnets [61]. The intermediate state mainly consists of virtual excitation from the occupied 97th MO to the unoccupied 112th and 114th MOs with coefficients 0.436 and 0.317, respectively. These are the d_K coefficients in Eq. (2). In contrast, the initial and final states mainly contain a virtual excitation from the occupied 109th MO to the unoccupied 110th MO [highest occupied molecular orbital and lowest unoccupied molecular orbital (HOMO and LUMO)] with a coefficient of -0.707. Since the correlational content (expressed through the respective virtual excitations) is different for the initial and the final states, the overlap between the intermediate and the initial states is not very strong, a fact which, in turn, leads to the weak transient population of the intermediate state. The spin-switching processes on the Hep-type $[Co\&B_{40}]^-$ optimized with 6-311G and LANL2dz basis set complete within 1 ps and are illustrated in Figs. 5(c) and 5(d), respectively. The longer time can be attributed to the involvement of more intermediate states (ten states in total). Three of them attain comparably higher populations than the aforementioned spin switching scenario, with maximal values 48.8%, 23.0%, and 37.8%, respectively. The energy differences between these three intermediate states and the initial state are 0.782, 0.783, and 0.784 eV, respectively. A detailed analysis shows that they stem from the same triplet state which mainly contains the virtual excitations from the occupied 74th and 90th MOs to the unoccupied 148th, 150th, 165th, and 167th MOs. The same four unoccupied MOs also contribute to the dominant virtual excitations of the initial and the final states. Therefore, the large overlap between the initial and the intermediate states explains the high transient population of the three intermediate states during the process. In addition, the strong competition between the final and the intermediate states is also at the origin of the lower spin switching speed. Note that the four unoccupied orbitals (148th, 150th, 165th, and 167th) are mainly composed of *d*-character atomic orbitals orbitals with coefficients 0.278, 0.234, 0.489, and 0.351, respectively (once again a manifestation that the spin-switching process is highly localized on the Co atom).

C. Structural optimization and spin dynamics of deformed $[Co\&B_{40}]^-$

To investigate the strain effect on the spin-dynamics features of the Hep-type $[Co\&B_{40}]^-$ system, we additionally apply both tensile and compressive strains on the system with a magnitude of 0.5% and 1.0% (Fig. 6). As mentioned previously, the maximum strain on the pure B_{40} structure before material failure sets in is much larger along the 6-6 than along the 7-7 direction. Therefore, the uniaxial strain is applied along the 6-6 direction. The optimization calculations are performed again to obtain the most stable distorted geometric structure (with the constraint of keeping the positions of the B atoms, on which the strain is applied, fixed). We find that the changes of the bond angle and the dihedral angle between two adjacent multimembered rings mainly dominate the geometric distortion on the Hep-type $[Co\&B_{40}]^-$, while the length of the B-B bond remains almost unchanged. The Co atom is still located near the center of heptagon at a distance of around 0.499 Å. In addition, the symmetry of the boron cage is lowered from D_{2d} to C_s, which is consistent with the symmetry reduction of the pristine B_{40}. For comparison, the total energy and the HOMO-LUMO energy gap for the equilibrium and distorted structures are listed in Table IV. As expected, the external strain can slightly break the geometric stability of Hep-type $[Co\&B_{40}]^-$ since the total energy increases with increasing tensile or compressive strain. Regarding the HOMO-LUMO energy difference, it is interesting that increasing the tensile strain results in the opening of the energy gap while increasing the compressive strain does the opposite. In other

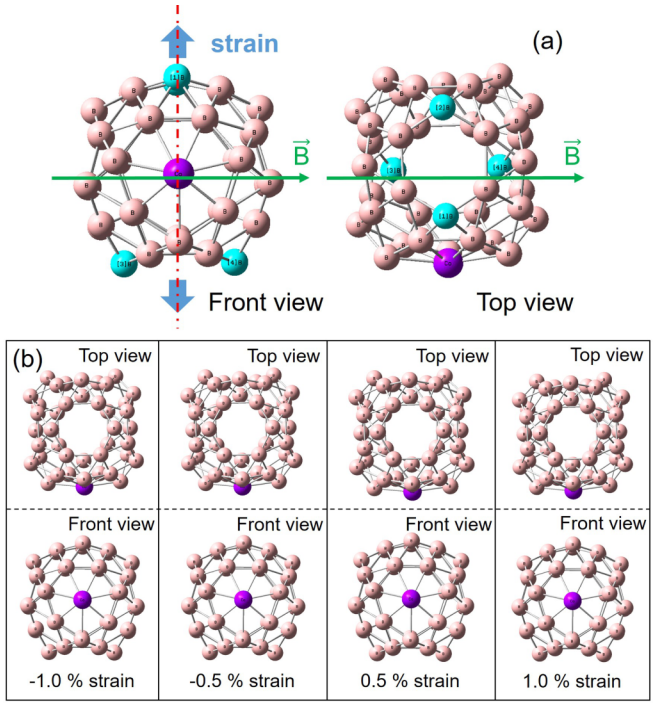

FIG. 6. Distorted structure of Hep-type $[Co\&B_{40}]^-$. (a) the orientation of applied uniaxial strain on $[Co\&B_{40}]^-$. The highlighted four atoms are the boron atoms on which the strain is applied. The blue arrows denote the direction of the uniaxial strain. The green arrows denote the direction of the external static magnetic field. (b) The optimized distorted structure of $[Co\&B_{40}]^-$. The applied strain shown in the panels from left to right is -1.0%, -0.5%, 0.5%, and 1.0%, respectively.

words, the local spin-switching is asymmetric with respect to tensile and compressive stress.

Similarly as in the undistorted structure, we calculate the spin density distribution of each excited state for the distorted structures. For the lowest triplet ground state (i.e., the first excited state), the spin density is always highly localized on the Co atom for each distorted structure, which means that neither tensile nor compressive strain can induce significant spin redistribution in $[Co\&B_{40}]^-$. The absolute values of the spin density on the Co atom with strain varying from -1.0% to 1.0% are 0.902, 0.905, 0.854, 0.894, and 0.899, respectively. The detailed analysis of the SAC-CI results reveals that this is mainly due to the invariance of the dominant virtual excitation (from HOMO to LUMO) of the lowest triplet state.

TABLE IV. The total energy (E_{tot}) and HOMO-LUMO energy gap ($\Delta E_{HOMO\text{-}LUMO}$) of equilibrium and distorted structures of Hep-type $[Co\&B_{40}]^-$.

Strain	E_{tot} (eV)	$\Delta E_{HOMO\text{-}LUMO}$ (eV)
-1.0%	-30414.923	5.777
-0.5%	-30414.934	5.772
0.0	-30414.937	5.769
0.5%	-30414.934	5.767
1.0%	-30414.923	5.762

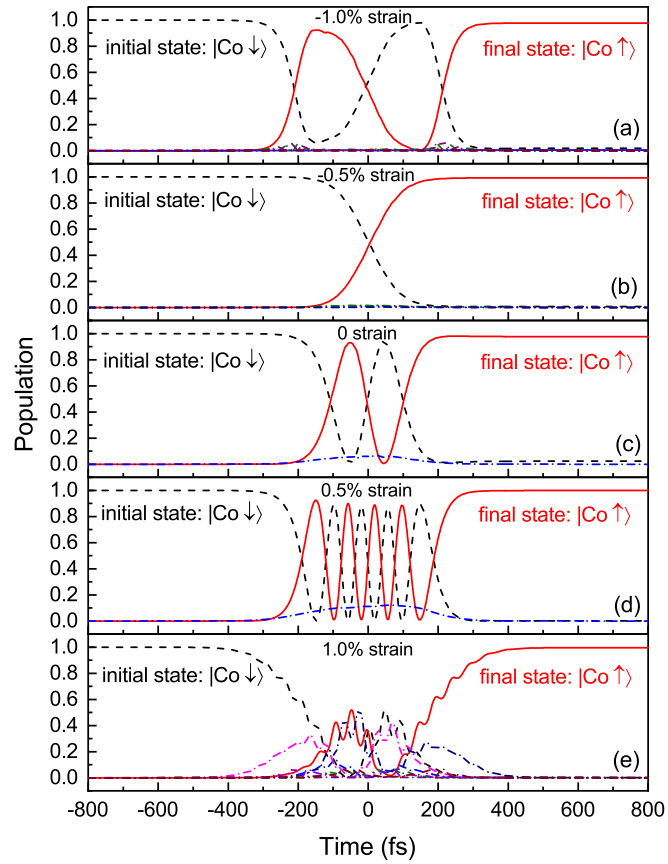

FIG. 7. Time evolution of electronic population of the initial (dashed black line), final (solid red line), and intermediate states (dash-dotted line in other colors) with the uniaxial strain of (a) -1.0%, (b) -0.5%, (c) 0.0, (d) 0.5%, and (e) 1.0% during the local spin-switching process at the Co atom of the exohedral Hep-type fullerene $[Co\&B_{40}]^-$ (cf. Fig. 6). $|Co\downarrow\rangle$ and $|Co\uparrow\rangle$ denotes the spin-down (initial) and spin-up (final) states with the spin density highly localized on the Co atom.

D. Strain modulation of spin dynamics on $[Co\&B_{40}]^-$

According to our calculations, the laser-induced ultrafast spin-switching process can be achieved on both the stretched and the compressed Hep-type $[Co\&B_{40}]^-$ systems. The applied uniaxial strain can significantly modify the duration and alter the intermediate states of the spin-switching process. Remarkably, Kirilyuk *et al.* also demonstrated that the permanent magnetization reversal can be modulated by the resonant excitation of anharmonic (out-of-plane) phonon modes in a garnet film [62]. It is quite similar to our system where we have the boron cage as sphere surface with uniaxial strain applied perpendicularly to it. Figures 7 and 8 illustrate the time evolution of the population of the involved electronic states and the expectation values of the spin components on all the distorted structures [for comparison the spin-switching scenario on the equilibrium structure is repeated in Figs. 7(c) and 8(c)]. The calculated oscillator strengths of the five structures are shown in Fig. 9, from which we can quantitatively estimate the coupling between the initial and other many-body states. The optimized laser parameters of each spin-switching scenario are listed in Table III. Inspection of the coefficients of

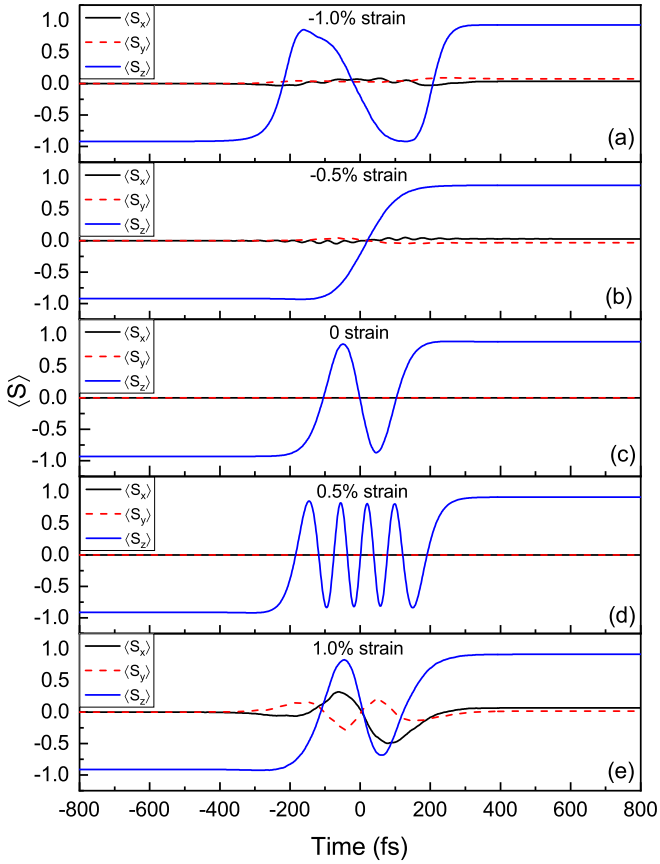

FIG. 8. Time-resolved expectation values of the spin components with the uniaxial strain of (a) −1.0%, (b) −0.5%, (c) 0.0, (d) 0.5%, and (e) 1.0%, respectively, during the local spin-switching process at the Co atom of the exohedral Hep-type fullerene $[Co\&B_{40}]^-$ (cf. Fig. 6).

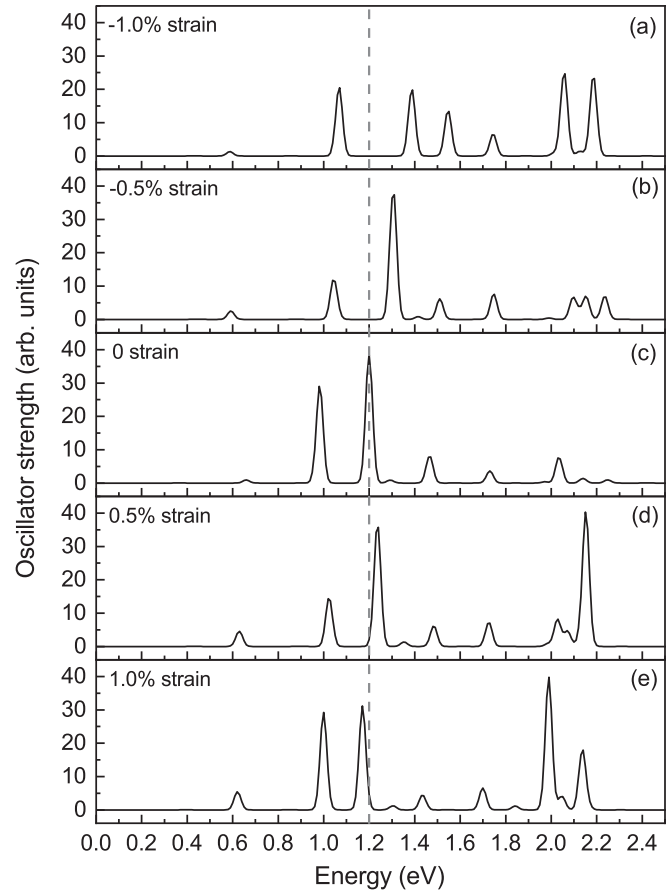

FIG. 9. The calculated electronic optical absorption spectra of the exohedral Hep-type fullerene $[Co\&B_{40}]^-$ at the SAC-CI level (see text). The abscissa denotes the energy difference between initial state and other many-body spin states. The ordinate denotes the oscillator strength. (a)–(e) denote the spectrum of structures with −1.0%, −0.5%, 0.0, 0.5%, and 1.0% strain, respectively (cf. Fig. 6). The dashed line serves as a guide to the eye and indicates the energy of the strongest absorption peak without any strain at 1.20 eV (see text).

all the virtual excitations for different tensile and compressive strains reveals that the virtual charge-transfer excitations (i.e., dynamical correlations) gain weight as the strain becomes stronger. This results in a slight spin redistribution which, in turn, has a dramatic effect upon the laser-induced spin dynamics. Therefore, the speed and efficiency of the spin-switching process on Hep-type $[Co\&B_{40}]^-$ can be manipulated by applied uniaxial strain. Furthermore, by comparing the population transfer shown in Fig. 7, we find that the tensile and compressive strains induce different modification scenarios on the spin-switching process.

For the tensile distortion, the increasing tensile strain along the 6-6 direction slows down the spin-switching process on Hep-type $[Co\&B_{40}]^-$. It takes around 600 and 800 fs for the spin-switching process to finish under the tensile strain of magnitude 0.5% and 1.0%, respectively (recall that the time needed to complete spin switching on the equilibrium structure is 500 fs). For 0.5% tensile strain, there is only one intermediate state involved in the spin-switching process (2.311 eV above the initial state). Similar to the spin-switching scenario of the equilibrium structure, the intermediate state gets only weakly populated. This state mainly contains a virtual excitation from the occupied 97th MO to the unoccupied 112th and 114th MOs with coefficients −0.443 and 0.287, respectively. It should be noted that the same virtual excitations also dominate the intermediate state of the switching process on the equilibrium structure. The initial and final states of the 0.5%-strain structure also mainly contain the virtual excitation from HOMO to LUMO with coefficient −0.654. Therefore, the similar initial, final, and intermediate states between the 0.5%-strain and the equilibrium structure ultimately lead to two very similar spin switching scenarios.

Regarding the structure under 1.0% tensile strain, there are, in total, seven intermediate states with relative energy 0.001, 2.164 (three degenerate triplet states), and 2.305 eV (three degenerate triplet states), respectively. Contrary to the weakly populated intermediate state on the 0.5%-strain structure, the maximum population of the intermediate states reaches 52.2%. Here, the dominant virtual excitations of the highest populated intermediate state and the initial state involve the same unoccupied MO (LUMO). This leads to the large overlap between the initial and intermediate states, and strong competition between the intermediate and final states as well, which finally results in the larger population of the

intermediate state and the longer duration of the spin-switching process. Understandably, these correlations variations for the different distorted structures also result into shifting of the peaks of their absorption spectra (Fig. 9), e.g., the shifting of the peak at 1.200 eV (indicated in Fig. 9 with a dashed line) which is significantly stronger for compressive 0.5% (1.310 eV) than for tensile 0.5% strain (1.240 eV). Interestingly, for weaker strains the peak gets blue-shifted for both strain directions, while for stronger strains the peak frequency increases for compressive strain (shift from 1.200 to 1.390 eV) and decreases for tensile strain (shift from 1.200 to 1.170 eV). The same effect can be observed for the peak at 1.470 eV.

As it turns out, the situation is different for the Hep-type $[Co\&B_{40}]^-$ under compressive strain. It takes about 600 fs to complete the spin-switching process under 1.0% strain, which is, as expected, slower than the switching process without strain. Nevertheless, 0.5% compressive strain results in a faster switching process that completes within 350 fs. This is also the fastest spin-switching process among all the scenarios on the Hep-type $[Co\&B_{40}]^-$ system. As shown in Fig. 7(b), the spin-switching process under 0.5% compressive strain involves four intermediate states. The energy differences between the four intermediate states and the initial state are 0.001 and 2.422 eV (there are three degenerate triplet states), respectively. The higher-energy intermediate states have similar electronic configuration to that of the equilibrium structure, and thus we attribute the higher spin-switching speed to the involvement of the energetically lower intermediate state. Blocking this state significantly suppresses the whole process, an effect which we regard as an extension of the blocking effect mentioned in the previous subsection.

With respect to the compressive strain with magnitude of 1.0%, similar to the switching process under 1.0% tensile strain, seven intermediate states are involved with 0.001 eV, 2.257 eV (three degenerate triplet states), and 2.422 eV (three degenerate triplet states) higher in energy than the initial state. However, the maximum population of these intermediate states only reaches 6.2%. This is mainly because in this distorted structure, the dominant virtual excitations of the largest populated intermediate states (from the 106th MO to the 115th MO and from the 97th MO to the 112th MO with amplitudes 0.531 and 0.385, respectively) are different from the initial state (from HOMO to LUMO with amplitude of 0.661). But at the same time, there are several virtual excitations including the HOMO and LUMO with amplitudes −0.179, −0.121, −0.111, −0.109, and 0.116, guaranteeing the appreciable overlap between the initial and the intermediate states. It ultimately leads to the competition between the final and the intermediate states and thus renders the whole switching process slower.

Summarizing the dynamic results for the various strains, probably the most striking difference in the spin-switching behavior is the number of (quasi-)Rabi cycles needed (Fig. 7). Without strain two cycles are needed. 0.5% compression reduces this number to only one cycle [Fig. 7(b)], while the same amount of extension necessitates four cycles [Fig. 7(d)]. This can be attributed to the fact that the external strain changes the dipole moment between the intermediate and final states, which, in turn, results in different frequency

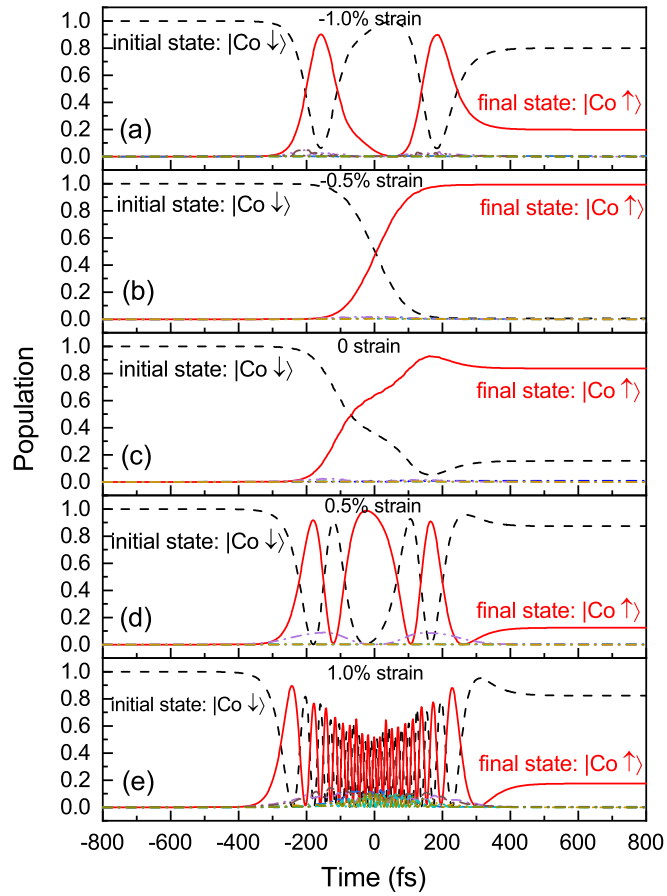

FIG. 10. Time evolution of electronic population of the initial (dashed black line), final (solid red line), and intermediate states (dash-dotted line in other colors) driven by the laser pulse which is optimized for −0.5% strain. The uniaxial strain applied here is (a) −1.0%, (b) −0.5%, (c) 0.0, (d) 0.5%, and (e) 1.0%, respectively. $|Co\downarrow\rangle$ and $|Co\uparrow\rangle$ denote the spin-down (initial) and spin-up (final) states with the spin density highly localized on the Co atom.

of the quasi-Rabi oscillation. For stronger strains, more intermediate states are involved in the spin-switching processes, and the interaction among these states tends to become more complicated. Therefore, the difference becomes even more dramatic, with the compressive strain retaining a fairly good resemblance to the unstrained case, while a tensile strain leads the whole process towards a more chaotic-like behavior [Figs. 7(a) and 7(e)].

In the aforementioned scenarios the laser pulse is reoptimized separately for each strain. Using the *same* laser parameters for all strains we see that the phonons can significantly enhance this nonlinear process. In Fig. 10 the laser parameters that were optimized for −0.5% strain [used in Figs. 7(b) and 8(b)], are also applied to our structure under different strains. We see that with the exception of the unstrained geometry, for which the fidelity still drops from more than 99% down to less than 84%, the process is almost completely suppressed. Using other laser parameters, it is possible to completely suppress the spin dynamics at the zero-strain structure as well (shown in Fig. S1 in the Supplemental Material [56]). Obviously, strain can play an important role in the manipulation and control of ultrafast laser-induced spin-dynamics processes.

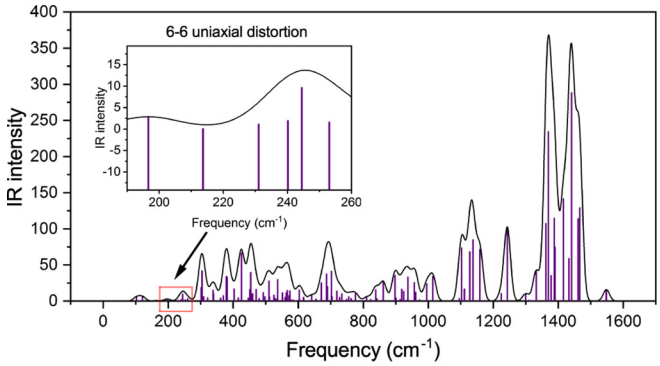

FIG. 11. Infrared (vibrational) spectrum of the Hep-type $[Co\&B_{40}]^-$ cluster at the HF level [cf. Fig. 4(b)]. The thin line includes an artificial Gaussian broadening of 23 cm^{-1} at half height, solely for visualization purposes.

E. Molecular vibrations of $[Co\&B_{40}]^-$

Besides external mechanical forces, strain can also be spontaneously generated by molecular vibrations. To study this we also look deeper into the geometric distortion, the vibronic period, and the amplitude of each normal mode and compare them with the 6-6 distorted structure. The infrared (vibrational) spectrum of the undistorted $[Co\&B_{40}]^-$ structure is presented in Fig. 11. A detailed analysis of the several normal modes reveals that the ones which most closely resemble the geometry distortion due to the 6-6 uniaxial strain are the modes with energies 197, 214, 240, 245, and 253 cm^{-1}, which are shown in the zoomed panel in Fig. 11, corresponding to vibronic periods of 170, 156, 139, 136, and 132 fs, respectively (the corresponding normal modes are illustrated in the Supplemental Material [56]). The results are comparable with the spin-dynamics processes achieved on $[Co\&B_{40}]^-$, which are also within the subpicosecond regime. After obtaining the reduced mass and the frequency of each normal mode from the classical frequency calculations, we use those values to canonically quantize the modes within the harmonic approximation (e.g., we treat them as quantum harmonic oscillators), and calculate the vibrational amplitude from the respective harmonic-oscillator wave functions (following Shankar's analysis, we consider the left-most and the right-most maxima of the probability density of the first excited state [63]). We find that the amplitude for the case of exactly one phonon is about 0.033 Å, a dislocation which equals 0.589% strain. This value, which of course becomes higher for elevated temperatures and more phonons, nicely matches the magnitude of the strain we applied in the spin-dynamics calculations. The detailed calculation is shown in the Supplemental Material [56].

For 300 K temperature, this value amounts to 0.14 Å dislocation and is comparable to the ones reported by Zhang *et al.* for C_{60} [64]. Obviously, due to the finiteness of our molecular system (phonon/vibron confinement), the normal modes also play an active role in the coherent regime of the laser-induced magnetization dynamics (contrary to the much slower phonons in extended systems, as discussed, e.g., by Bigot *et al.* [65]). At room temperature, these normal modes have a population around 0.03, and, as it turns out, they can even assist the process further by providing additional channels which can act as phonon-dressed intermediate states, thus speeding up the result while at the same time help avoid a significant increase of the electronic temperature. Furthermore, the tension-compression asymmetry (be it strain or phonon induced) indicates a strong anharmonicity of the vibrational modes of the system, which, if properly exploited, can give rise to irreversible processes, needed for the initiation of any logic computation [66] or one-way quantum computing [67]. The detailed results on the propagations including coherent vibrational modes go beyond the scope of the current paper and will be published elsewhere.

IV. CONCLUSION

In conclusion, the elastic properties of B_{40} and spin-dynamics properties of $[Co\&B_{40}]^-$ are systematically investigated with *ab initio* calculations. The following conclusions can be drawn in this paper.

(i) The pristine B_{40} exhibits strong ductility under both uniaxial tension and compression. The magnitude of the ultimate uniaxial distortion on B_{40} strongly depends on the direction of the applied strain, indicating the mechanical anisotropy of B_{40}.

(ii) The spin density is highly localized on the Co atom embedded in the exohedral fullerene $[Co\&B_{40}]^-$, and the laser-induced ultrafast spin-switching process can be achieved on the $[Co\&B_{40}]^-$ system within 600 fs.

(iii) The spin-switching process propagated on $[Co\&B_{40}]^-$ can be dramatically modulated by varying the magnitude of the strain. Particularly, the tensile and compressive processes can result in different modulation scenarios on the spin dynamics. The fastest spin-switching process takes place on the structure under 0.5% compressive strain within 350 fs.

The investigations already demonstrated that magnetic molecules and the straintronic mechanism hold great promise for realizing the basic elements of high-performance nanoscale devices, such as transistors, memristors and gyrators [14–19,25,26]. Through our investigation, we go further and combine a magnetic molecule, spin dynamics, and straintronics to explore the strain-modulated spin-dynamics processes. This extra step is expected to reveal the mechanism of the strain-modulated ultrafast spin-dynamics properties of exohedral fullerenes, and to establish the theoretical basis and novel ideas for the design of functional spin devices based on the exohedral fullerenes.

ACKNOWLEDGMENTS

This work is supported by the National NSF (Grants No. 11872309, No. 11572251, and No. 11504223) of China, the Natural Science Basic Research Plan in Shaanxi Province (Grants No. 2020JM-120 and No. 2017JM1033), and the Fundamental Research Funds for the Central Universities (Grants No. 3102017JC01003 and No. GK201903015) of China. C.L. acknowledges the financial support from the program of China Scholarships Council (Grant No. 201906295029). G.L. thankfully acknowledges the hospitality of NPU during the summer semester 2019.

[1] S. I. Rao, C. Woodward, B. Akdim, E. Antillon, T. A. Parthasarathy, J. A. El-Awady, and D. M. Dimiduk, Acta Mater. **164**, 171 (2019).

[2] L. Zhang, W. Geng, C. Tong, X. Chen, T. Cao, and M. Chen, Sci. Rep. **8**, 7760 (2018).

[3] M. S. Si, J. Y. Li, D. S. Xue, and G. P. Zhang, Phys. Rev. B **88**, 144425 (2013).

[4] R. Torchio, Y. O. Kvashnin, S. Pascarelli, O. Mathon, C. Marini, L. Genovese, P. Bruno, G. Garbarino, A. Dewaele, F. Occelli, and P. Loubeyre, Phys. Rev. Lett. **107**, 237202 (2011).

[5] D. Kumar, A. David, A. Fouchet, A. Pautrat, J. Varignon, C. U. Jung, U. Lüders, B. Domengès, O. Copie, P. Ghosez, and W. Prellier, Phys. Rev. B **99**, 224405 (2019).

[6] Z. Wu, J. Yu, and S. Yuan, Phys. Chem. Chem. Phys. **21**, 7750 (2019).

[7] S. Jethva, S. Katba, M. Bhatnagar, M. Ranjan, D. Shukla, and D. G. Kuberkar, J. Appl. Phys. **125**, 082510 (2019).

[8] M. Gu, Q. Xie, X. Shen, R. Xie, J. Wang, G. Tang, D. Wu, G. P. Zhang, and X. S. Wu, Phys. Rev. Lett. **109**, 157003 (2012).

[9] C. Fourmental, S. Mondal, R. Banerjee, A. Bellec, Y. Garreau, A. Coati, C. Chacon, Y. Girard, J. Lagoute, S. Rousset, M. Boillot, T. Mallah, C. Enachescu, C. Barreteau, Y. J. Dappe, A. Smogunov, S. Narasimhan, and V. Repain, Phys. Chem. Lett. **10**, 4103 (2019).

[10] Q. Deng and A. Popov, J. Am. Chem. Soc. **136**, 4257 (2014).

[11] O. Tishchenkoa, R. Li, and D. G. Truhlar, Proc. Natl. Acad. Sci. USA **107**, 19139 (2010).

[12] A. Popov, C. Chen, S. Yang, F. Lipps, and L. Dunsch, ACS Nano **4**, 4857 (2010).

[13] W. Jin, C. Li, G. Lefkidis, and W. Hübner, Phys. Rev. B **89**, 024419 (2014).

[14] A. A. Bukharaev, A. K. Zvezdin, A. P. Pyatakov, and Y. K. Fetisov, Phys.-Usp. **61**, 1175 (2018).

[15] J. H. Lee, L. Fang, E. Vlahos, X. Ke, Y. W. Jung, L. F. Kourkoutis, J.-W. Kim, P. J. Ryan, T. Heeg, M. Roeckerath, V. Goian, M. Bernhagen, R. Uecker, P. C. Hamme, K. M. Rabe, S. Kamba, J. Schubert, J. W. Freeland, D. A. Muller, C. J. Fennie, P. Schiffer, V. Gopalan, E. Johnston-Halperin, and D. G. Schlom, Nature **466**, 954 (2010).

[16] N. Levy, S. A. Burke, K. L. Meaker, M. Panlasigui, A. Zettl, F. Guinea, A. H. C. Neto, and M. F. Crommie, Science **329**, 544 (2010).

[17] D. E. Nikonov and I. A. Young, J. Mater. Res. **29**, 2109 (2014).

[18] V. Iurchuk, B. Doudin, and B. Kundys, J. Phys. Condens. Matter **26**, 292202 (2014).

[19] W. Hou, A. Ayiyimanesh, A. Sewaket, T. Peña, C. Watson, M. Liu, H. Askari, and S. M. Wu, Nat. Nanotech. **14**, 668 (2019).

[20] H. Xiang, G. Lefkidis, and W. Hübner, Phys. Rev. B **86**, 134402 (2012).

[21] Y. Yokoyama, Y. Yamasaki, M. Taguchi, Y. Hirata, K. Takubo, J. Miyawaki, Y. Harada, D. Asakura, J. Fujioka, M. Nakamura, H. Daimon, M. Kawasaki, Y. Tokura, and H. Wadati, Phys. Rev. Lett. **120**, 206402 (2018).

[22] B. Xu, X. Xiao, and N. J. Tao, J. Am. Chem. Soc. **125**, 16164 (2003).

[23] M. Frei, S. V. Aradhya, M. Koentopp, M. S. Hybertsen, and L. Venkataraman, Nano Lett. **11**, 1518 (2011).

[24] H. Rascón-Ramos, J. M. Artés, Y. Li, and J. Hihath, Nat. Mater. **14**, 517 (2015).

[25] R. Vincent, S. Klyatskaya, M. Ruben, W. Wernsdorfer, and F. Balestro, Nature **488**, 357 (2012).

[26] H. A. Bustami, G. Koplovitz, D. Primc, S. Yochelis, E. Capua, D. Porath, R. Naaman, and Y. Paltiel, Small **14**, 1801249 (2018).

[27] Throughout the paper the signs @ and & are used for the endohedral and exohedral fullerenes, respectively.

[28] Z. Y. Wang, K. H. Su, H. Q. Fan, L. D. Hu, X. Wang, Y. L. Li, and Z. Y. Wen, Comput. Mater. Sci. **40**, 537 (2007).

[29] J. Niklas, K. L. Mardis, and O. G. Poluektov, J. Phys. Chem. Lett. **9**, 3915 (2018).

[30] C. Li, J. Liu, S. Zhang, G. Lefkidis, and W. Hübner, Carbon **87**, 153 (2015).

[31] J. Zhao, L. Ma, D. Tian, and R. Xie, J. Comput. Theor. Nanosci. **5**, 7 (2008).

[32] Z. G. Fthenakis, R. W. A. Havenith, M. Menon, and P. W. Fowler, Phys. Rev. B **75**, 155435 (2007).

[33] G. Seifert, T. Heine, and P. W. Fowler, Eur. Phys. J. D **16**, 341 (2001).

[34] H. J. Zhai, Y. F. Zhao, W. L. Li, Q. Chen, H. Bai, H. S. Hu, Z. A. Piazza, W. J. Tian, H. G. Lu, Y. B. Wu, Y. W. Mu, G. F. Wei, Z. P. Liu, J. Li, S. D. Li, and L. S. Wang, Nat. Chem. **6**, 727 (2014).

[35] H. Bai, Q. Chen, H. J. Zhai, and S. D. Li, Angew. Chem. Int. Ed. **54**, 941 (2015).

[36] W. Fa, S. Chen, S. Pande, and X. C. Zeng, J. Phys. Chem. A **119**, 11208 (2015).

[37] P. Jin, Q. Hou, and C. Tang, Theor. Chem. Acc. **134**, 13 (2015).

[38] S. Li, Z. Zhang, Z. Long, and D. Chen, ACS Omega **4**, 5705 (2019).

[39] C. Liu, X. Ye, X. Wang, and X. Yan, RSC Adv. **6**, 56907 (2016).

[40] H. Dong, T. Hou, S. T. Lee, and Y. Li, Sci. Rep. **5**, 09952 (2015).

[41] B. Lin, H. Dong, C. Du, T. Hou, H. Lin, and Y. Li, Nanotechnology **27**, 075501 (2016).

[42] X. Sun, S. Cheng, and X. Feng, Ionics **25**, 3413 (2019).

[43] H. Dong, B. Lin, K. Gilmore, T. Hou, S. T. Lee, and Y. Li, Curr. Appl. Phys. **15**, 1084 (2015).

[44] G. Gao, F. Ma, Y. Jiao, Q. Sun, Y. Jiao, E. Waclawik, and A. Du, Comput. Mater. Sci. **108**, 38 (2015).

[45] H. Nakatsuji, Chem. Phys. Lett. **67**, 329 (1979).

[46] M. J. Frisch, G. W. Trucks, H. B. Schlegel, G. E. Scuseria, M. A. Robb, J. R. Cheeseman, G. Scalmani, V. Barone, B. Mennucci, G. A. Petersson, H. Nakatsuji, M. Caricato, X. Li, H. P. Hratchian, A. F. Izmaylov, J. Bloino, G. Zheng, J. L. Sonnenberg, M. Hada, M. Ehara, K. Toyota, R. Fukuda, J. Hasegawa, M. Ishida, T. Nakajima, Y. Honda, O. Kitao, H. Nakai, T. Vreven, J. A. Montgomery, J. E. Peralta, F. Ogliaro, M. Bearpark, J. J. Heyd, E. Brothers, K. N. Kudin, V. N. Staroverov, R. Kobayashi, J. Normand, K. Raghavachari, A. Rendell, J. C. Burant, S. S. Iyengar, J. Tomasi, M. Cossi, N. Rega, J. M. Millam, M. Klene, J. E. Knox, J. B. Cross, V. Bakken, C. Adamo, J. Jaramillo, R. Gomperts, R. E. Stratmann, O. Yazyev, A. J. Austin, R. Cammi, C. Pomelli, J. W. Ochterski, R. L. Martin, K. Morokuma, V. G. Zakrzewski, G. A. Voth, P. Salvador, J. J. Dannenberg, S. Dapprich, A. D. Daniels, Ö. Farkas, J. B. Foresman, J. V. Ortiz, J. Cioslowski, and D. J. Fox, GAUSSIAN 09 Revision A.2 (2009).

[47] A. I. Krylov, Annu. Rev. Phys. Chem. **59**, 433 (2008).

[48] P. J. Hay and W. R. Wadt, J. Chem. Phys. **82**, 299 (1985).

[49] G. Lefkidis and W. Hübner, Phys. Rev. Lett. **95**, 077401 (2005).

[50] G. Lefkidis and W. Hübner, Phys. Rev. B **76**, 014418 (2007).
[51] G. Lefkidis, G. P. Zhang, and W. Hübner, Phys. Rev. Lett. **103**, 217401 (2009).
[52] G. Lefkidis, and W. Hübner, Phys. Rev. B **87**, 014404 (2013).
[53] B. W. Shore, K. Bergmann, A. Kuhn, S. Schiemann, J. Oreg, and J. H. Eberly, Phys. Rev. A **45**, 5297 (1992).
[54] C. Li, T. Hartenstein, G. Lefkidis, and W. Hübner, Phys. Rev. B **79**, 180413(R) (2009).
[55] T. Hartenstein, C. Li, G. Lefkidis, and W. Hübner, J. Phys. D: Appl. Phys. **41**, 164006 (2008).
[56] See Supplemental Material at http://link.aps.org/supplemental/10.1103/PhysRevB.102.024416 for the detailed structural parameters of B_{40} and $[Co\&B_{40}]^-$, the suppressed spin-switching processes at the zero-strain $[Co\&B_{40}]^-$ induced by different laser pulses, and the detailed derivation of amplitude of quantum harmonic oscillator $[Co\&B_{40}]^-$ system analogous to the classical normal mode.
[57] C. Li, J. Liu, G. Lefkidis, and W. Hübner, Phys. Chem. Chem. Phys. **19**, 673 (2017).
[58] C. Li, J. Liu, S. Zhang, G. Lefkidis, and W. Hübner, IEEE Trans. Magn. **51**, 2900505 (2015).
[59] C. Li, S. Zhang, W. Jin, G. Lefkidis, and W. Hübner, IEEE Trans. Magn. **49**, 3195 (2013).
[60] C. Li, W. Jin, H. Xiang, G. Lefkidis, and W. Hübner, Phys. Rev. B **84**, 054415 (2011).
[61] W. Jin, F. Rupp, K. Chevalier, M. M. N. Wolf, M. C. Rojas, G. Lefkidis, H. J. Krüger, R. Diller, and W. Hübner, Phys. Rev. Lett. **109**, 267209 (2012).
[62] C. S. Davies, K. H. Prabhakara, M. D. Davydova, K. A. Zvezdin, T. B. Shapaeva, S. Wang, A. K. Zvezdin, A. Kirilyuk, Th. Rasing, and A. V. Kimel, Phys. Rev. Lett. **122**, 027202 (2019).
[63] R. Shankar, *Principles of Quantum Mechanics*, 2nd ed. (Kluwer Academic/Plenum, New York, 2011), p. 202.
[64] G. P. Zhang, X. Sun, T. F. George, and L. N. Pandey, J. Chem. Phys. **106**, 6398 (1997).
[65] J.-Y. Bigot, M. Vomir, and E. Beaurepaire, Nat. Phys. **5**, 515 (2009).
[66] C. Li, S. Zhang, W. Jin, G. Lefkidis, and W. Hübner, Phys. Rev. B **89**, 184404 (2014).
[67] P. Walther, K. J. Resch, T. Rudolph, E. Schenck, H. Weinfurter, V. Vedral, M. Aspelmeyer, and A. Zeilinger, Nature **434**, 169 (2005).